2002-08-01

Construction and Testing of a Low-Finesse Fabry-Perot Interferometer For Use in Atomic Spectroscopy

Nathan C. Moody

CONSTRUCTION AND TESTING OF A LOW-FINESSE FABRY-PEROT INTERFEROMETER FOR USE IN ATOMIC SPECTROSCOPY

by

Nathan C. Moody

Submitted to the Department of Physics and Astronomy in partial fulfillment of graduation requirements for the degree of

Bachelor of Science

Brigham Young University

August 2002

Advisor: Scott Bergeson

Signature: ____________________________

Thesis Coordinator: Justin Peatross

Signature: ______________________________

Department Chair: R. Steven Turley

Signature: ____________________________

Abstract

I built a low-finesse confocal cavity with aluminum mirrors for use in the imaging of ultra-cold calcium ion plasmas. The confocal cavity provides stability at large mirror separations, a condition necessary for achieving both low finesse and narrow peak widths. Additionally, the finesse in the case of coherent input is effectively doubled compared to multi-mode resonance. The cavity was tested using a GaN diode laser input at 397nm. The transmission obtained indicated that the finesse of the cavity was slightly lower than the prediction based on measurements of the mirror reflectivities and the assumption of incoherent input.

Acknowledgements

Special thanks go to Michael Lines and MOXTEK Inc. for depositing beautiful aluminum coatings onto the lenses. I am indebted to Diana and Brynner for their patience and endurance during a period when I was not able to be home as often as I should have been. I want to thank Dr. Scott Bergeson for encouraging me throughout the duration of this project and for the time he has spent helping me edit this work. Finally, I wish to express appreciation for my parents who have taught me to have confidence in my abilities; they are the reason for my attending this great university in the first place.

CONTENTS

LIST OF FIGURES

CHAPTER I. INTRODUCTION

1.1 Overview

The tuning of a diode laser to the precision necessary for the imaging of ultra-cold ion plasmas requires an instrument capable of resolving very small changes in frequency. Though several different types of reference cells may be used, a Fabry-Perot (FP) interferometer constructed of partially reflecting aluminum mirrors is particularly versatile because of aluminum's broadband reflectivity. I built a low-finesse confocal cavity with aluminum mirrors for use in the imaging of ultra-cold calcium ion plasmas.

High-finesse parallel plane cavities are simple to construct and align, and peak widths in the MHz range are easily achieved. On the other hand, low-finesse transmission with equally narrow peak widths requires the use of one or two concave mirrors in order to allow larger mirror separations.

My first objective is to provide a readily accessible discussion of the theory associated with the use of the confocal cavity. To accomplish this goal, I will first give a derivation of several important properties of the parallel plane FP cavity, including the reflecting finesse, the free spectral range, and the peak width. I focus here on pointing out the consequences of mirror reflectance and separation distance in terms of their relationship to finesse and peak width. I then discuss the significance of cavity modes and explain the two types of degeneracy in which all modes contribute to either "even" or "odd" peaks in the case of incoherent input. This is followed by an explanation of a technique used to match the divergence of the Gaussian mode to the curved mirror surface. A derivation of the finesse of a confocal cavity using ray theory completes the theoretical treatment.

My second objective is to describe the methods I used to construct and test our confocal FP interferometer and explain the results obtained. In Chapter II, I describe diode laser operation using both the Littrow and Littman-Metcalf external cavities, followed by a brief discussion of the deposition and testing of the aluminum films. Methods used to construct the FP interferometer and align the laser are described and illustrated at the end of the chapter. Results are presented and discussed in Chapter III.

1.2 Cavity stability

While both simple and well suited to many applications, the plane parallel FP cavity is limited by instability at large mirror separations. As the mirror spacing increases, it becomes increasingly difficult to align a laser beam to the precision necessary to contain the beam in the cavity. This problem was addressed in the mid-1950s when Pierre Connes suggested the possibility of employing spherical mirrors to construct a more stable instrument [1]. The spherical design, as well as other configurations using curved mirrors in combination with flat mirrors or mirrors of differing curvature, has made it possible to achieve stability with much longer cavities.

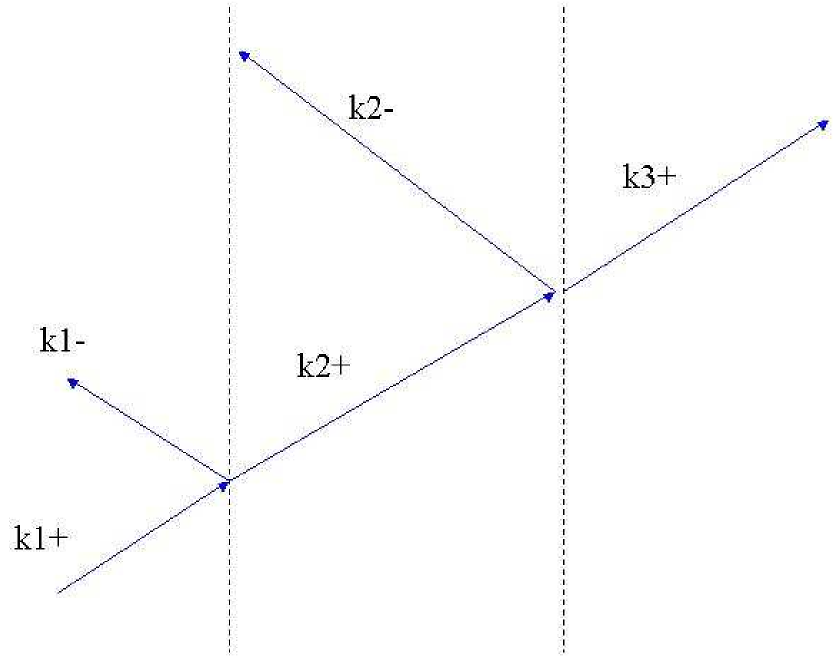

Fig. 1. Plane wave propagation vectors in the double boundary problem. Note that angles from normal are grossly exaggerated. Adapted from [2].

1.3 The parallel plane FP

This section is intended to provide a foundation of theory that will later be compared to the case of the confocal cavity. Much of the treatment here is similar to that found in [2]. Several important properties of the parallel plane cavity can be derived by approaching it as a double boundary problem. In the discussion that follows, the input of the cavity is assumed to be collimated and at normal incidence. A simple analysis can be accomplished by writing equations connecting the five plane waves shown in Fig. 1 in terms of Fresnel coefficients and phase factors [2]. The three resulting equations are then combined and written as the ratio of the transmitted electric field to the incident field, and an expression for the fraction of transmitted power at near-normal incidence easily follows. For lossless mirrors of equal reflectance *R* and transmission *T*, the transmission T_c of the cavity can be written [2] simply as

$$T_c = \frac{T_c \max}{1 + F \sin^2(\frac{\phi}{2})}, \tag{1}$$

where

$$T_c \max = \frac{T^2}{(1-R)^2}, \tag{2}$$

$$F = \frac{4R}{(1-R)^2}, \tag{3}$$

and ϕ is the phase shift due to a single round trip plus a constant phase factor that can be neglected in this analysis without any loss of validity. The factor *F* is called the finesse coefficient.

Several properties of interest can be derived directly from Eqs. 1 - 3. By inspection of Eq.1, the condition for resonance (maximum transmission) is $\phi = 2n\pi$, where n is an integer. (By the way, combining this relationship with Eq. 6 yields the intuitive condition for constructive interference, namely, $2L = n\lambda$) We set the expression for T_c equal to $T_c \max/2$ and make the substitution $\phi = \phi_0 + \phi_{FWHM}/2$, where ϕ_0 satisfies the resonance condition. It now becomes a simple matter to solve for the width of the transmission peak (the full width at half-maximum, to be precise) in units of radians. The result [2] is

$$\phi_{FWHM} = 4\sin^{-1}\frac{1}{\sqrt{F}}. \qquad (4a)$$

To the extent that $\sqrt{F} >> 1$, we can conveniently approximate the peak width as follows:

$$\phi_{FWHM} \cong \frac{4}{\sqrt{F}} = \frac{2(1-R)}{\sqrt{R}}. \qquad (4b)$$

Another important property of an FP cavity is a dimensionless quantity called the reflecting finesse, which is the ratio of the period to the peak width. Unfortunately, no consensus has been reached on the symbol that should be used to denote finesse; at least three are currently in use, including *f*, *N*, and $\Im$. I will use $\Im$. The finesse is given [2] by

$$\Im = \frac{2\pi}{\phi_{FWHM}} \cong \frac{\pi\sqrt{F}}{2} = \frac{\pi\sqrt{R}}{(1-R)}. \qquad (5)$$

These last two quantities, the peak width given in radians and the finesse, are both dependent only on the reflectance *R*.

We will now show that the free spectral range (FSR), which is expressed as either the change in frequency or wavelength corresponding to one full period of the transmission signal ($\Delta\phi = 2\pi$), is inversely proportional to the mirror separation *L*. To do this, we must first write an expression for ϕ in terms of *L* and the wavelength λ_0. The number of periods N_{plane} in a single round trip distance 2*L* is simply $2L/\lambda_0$.

Therefore, the phase shift ϕ after one round trip in the cavity is given by

$$\phi = \frac{2\pi}{period} * N_{plane}\, periods = \frac{4\pi L}{\lambda_0}. \tag{6}$$

Taking the derivative of Eq. 6 with respect to λ_0, inverting both sides, and multiplying by the differential $\partial\phi$, we obtain the following equation relating a change in wavelength to its corresponding change in the round trip phase shift:

$$\partial\lambda = \frac{(\lambda_0^{\ 2})}{4\pi L}\partial\phi. \tag{7}$$

We omit the minus sign since we are only concerned with the magnitude of $\partial\lambda$. After changing the differentials to finite quantities and making the substitution $\Delta\phi = 2\pi$, we find that the free spectral range of the FP cavity is given by

$$\Delta\lambda_{FSR} = \frac{\lambda_0^{\ 2}}{2L}. \tag{8a}$$

It is customary to express this quantity as a shift in frequency; the FSR is thus more commonly given as

$$\Delta\nu_{FSR} = \frac{c}{2L}. \tag{8b}$$

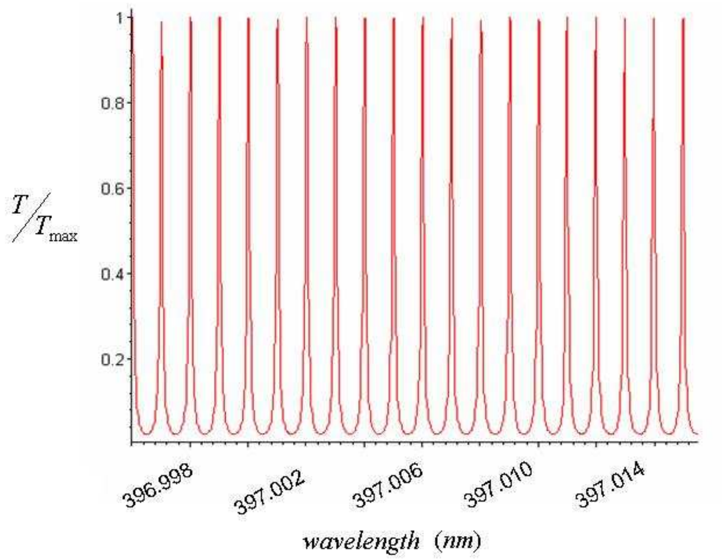

Fig. 2a. Low finesse cavity transmission with peak width of 190MHz. The mirror separation would have to be 7.9cm to achieve this signal using a parallel plane FP cavity.

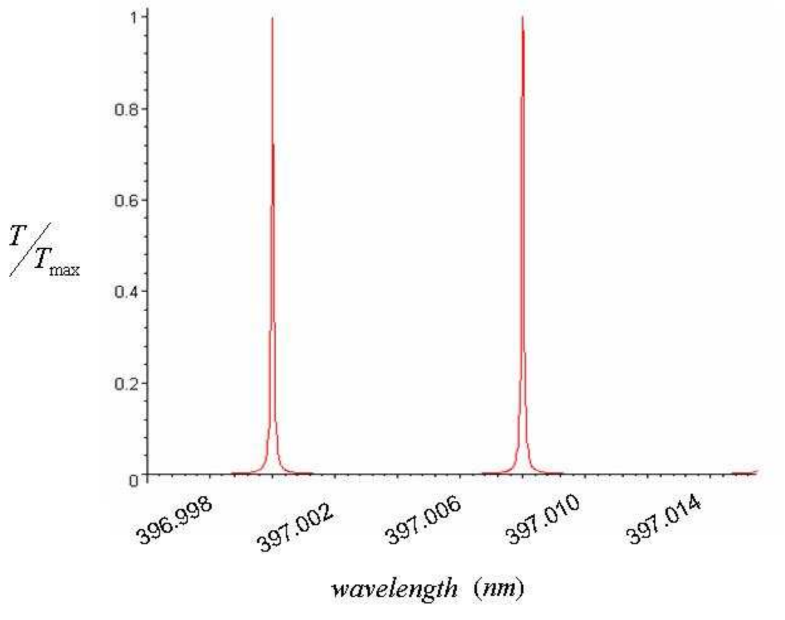

Fig. 2b. High finesse cavity transmission with the same peak width as in Fig. 2a. This signal may be obtained with a parallel plane cavity with a mirror spacing of 1.0cm.

Finally, we can solve for the peak width $\Delta\nu_{FWHM}$ using Eqs. 5, 8*a*, and the relationship $\Im = \frac{\Delta\nu_{FSR}}{\Delta\nu_{FWHM}}$. We find that it is inversely proportional to both $\sqrt{F}$ and the cavity length:

$$\Delta\nu_{FWHM} = \frac{c}{\pi L\sqrt{F}}. \tag{9}$$

Consider now the effect of *F* on the finesse and the peak width. The finesse goes like $\sqrt{F}$ while the peak width goes like $1/\sqrt{F}$. It follows that larger mirror reflectance gives rise to transmission spikes that are both narrow in absolute linewidth (small $\Delta\nu_{FWHM}$) and narrow compared to the period (high $\Im$). For our purposes, however, we needed an instrument that would give a narrow peak width but also have a *low* finesse $\Im$. A small finesse requires that *F* be small, which has the effect of broadening the transmission peaks. Hence, the cavity length needed to be increased (by inspection of Eq. 9) far beyond the limit of stable operation in order to keep $\Delta\nu_{FWHM}$ small. In particular, we needed an FP with a finesse of ~10 and a peak width of ~200MHz, corresponding to a mirror separation of ~10cm. Figs. 2*a* and 2*b* both show the transmission of a parallel plane FP with a peak width of 190MHz having a finesse of 10 and 100 respectively. The required plate separation to obtain the low-finesse transmission of Fig. 2*a* would be 7.9cm, an unstable condition for a plane parallel cavity. Consequently, the parallel plane cavity was ill suited for our purpose.

The theory of the parallel plane cavity is similar in many respects to that of the confocal cavity, but important differences exist. A discussion of cavity modes is prerequisite to the proper treatment of these differences.

1.4 Cavity modes

Modes are standing electric field distributions inside the cavity that satisfy the wave equation and the condition that the field must vanish at the mirrors. The following discussion is intended to provide a conceptual understanding of cavity modes, but the quantitative results derived are only valid for the case of a plane parallel Fabry-Perot. The derivation of resonance conditions for the confocal cavity is quite involved, so the results will only be stated at the end of this section. It is also beyond the scope of this treatment to provide many of the details of the simpler parallel plane case, such as the derivation of the electric field. The problem, however, is a classic case that can be found in many sources. Much of this treatment will follow the discussion provided in [3].

We consider first the case of a rectangular box cavity and later extend the results to the case of an open cavity having only the two ends. The electric field allowed to exist in the rectangular box is given [3] by

$$\begin{aligned} E_x &= e_x \cos k_x x * \sin k_y y * \sin k_z z * \sin \omega t \\ E_y &= e_y \sin k_x x * \cos k_y y * \sin k_z z * \sin \omega t \\ E_z &= e_z \sin k_x x * \sin k_y y * \cos k_z z * \sin \omega t \end{aligned} \quad , \tag{10}$$

where

$$\omega = ck \tag{11}$$

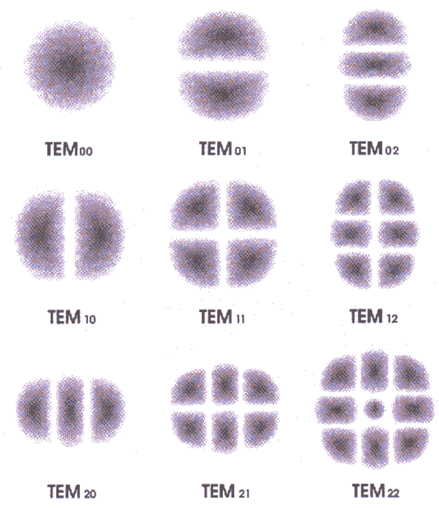

Fig. 3. Spatial mode intensity patterns. The first and second subscript digits indicate the number of nodes on the horizontal and vertical axes respectively. Nodes are manifest as minima in the intensity. Reproduced from [4].

and

$$k^2 = k_x^{\ 2} + k_y^{\ 2} + k_z^{\ 2}. \tag{12}$$

Applying the boundary condition that the field must vanish at the walls results in discrete allowable values for the components of the propagation vector, namely [3],

$$\begin{aligned} k_x &= \frac{l\pi}{2a} \\ k_y &= \frac{m\pi}{2a} \\ k_z &= \frac{n\pi}{L} \end{aligned} \tag{13}$$

where l, m, and n are positive integers, L is the length of the cavity, and a is the width of the sides of the cavity. It is important to note that the integers l, m, and n represent the number of nodes of a given mode along the x, y, and z-axes respectively. The nodes of a $TEM_{l,m}$ spatial mode are manifest as minima in the transmitted intensity pattern. For example, the TEM_{10} mode intensity pattern shown in Fig. 3 has a single node at $x = 0$.

In general, modes identified by *l* and *m* without regard to *n* are referred to as transverse modes. Similarly, modes with the same values for *l* and *m* having different values for *n* are designated as longitudinal (or axial) modes of the given transverse mode.

Now we consider modes where $l, m << n$, a condition that is satisfied by laser light propagating along the z-axis, say, between two parallel mirrors. Intuitively, we can safely expect that the absence of the sides of the box will make little difference since small *l* and *m* imply that the beam travels parallel to the z-axis. In this regime, the frequency of the light determines the nearest value of *n* that can resonate in the cavity, while the beam profile determines the values for *l* and *m* for a given resonant frequency. For this reason, longitudinal modes are often referred to as “frequency” modes, while transverse modes are often called “spatial” modes.

To find the resonant frequencies for a given mode, we only need to combine Eqs. 11 and 12 and solve for ν. We find that the resonant frequencies are given by

$$\nu = \frac{c}{2}[(\frac{n}{L})^2 + (\frac{m}{2a})^2 + (\frac{l}{2a})^2]^{\frac{1}{2}}. \tag{14}$$

A power series expansion of the radicand yields a more convenient approximation for the resonant frequencies, namely [3],

$$\nu \cong \frac{c}{2}(\frac{n}{L} + \frac{1}{2}\frac{(l^2 + m^2)}{n}\frac{L}{4a^2}). \tag{15}$$

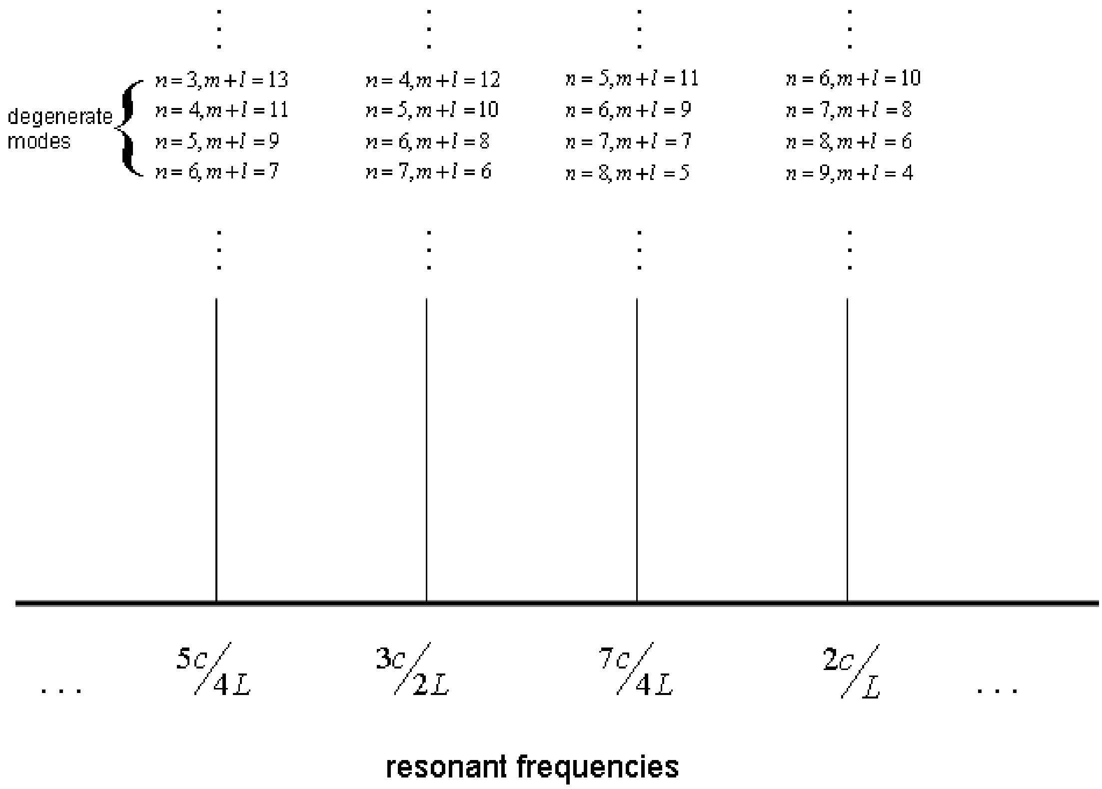

Fig. 4. Degeneracy of modes in the confocal cavity. Nearly all modes are degenerate with other modes having either odd or even values of $m + l$.

For a given spatial mode, the frequency difference between consecutive longitudinal modes ($\Delta n = 1$) is $\Delta\nu = c/2L$. This, of course, agrees with the free spectral range of the parallel plane cavity as derived in section 1.3. The frequency spacing between two consecutive spatial modes ($\Delta m = 1$ or $\Delta l = 1$) of a given longitudinal mode is much smaller, given [3] by

$$\Delta\nu = \frac{cL}{8na^2}(m + \frac{1}{2}). \tag{16}$$

We can conclude that the combination of a low-finesse cavity and spatially incoherent input would result in the transmission peaks of several spatial modes overlapping each other. This was not a significant concern for our low-finesse cavity, however, because the frequency spacing between consecutive spatial modes in a confocal cavity is much greater. The resonant frequencies for a confocal cavity are given [3] by

$$\nu = \frac{c[2n + (1 + m + l)]}{4L}. \tag{17}$$

It follows that the frequency spacing between consecutive spatial modes ($\Delta m = 1$ or $\Delta l = 1$) is $c/4L$, while the free spectral range ($\Delta n = 1$) is $c/2L$ as in the case of a parallel plane FP.

It is important to note the frequency degeneracy of the spatial modes, illustrated in Fig. 4. Modes having the same values for $2n + l + m$ have the same resonant frequency, hence the transmitted intensity of a given resonant frequency will be the sum of intensities transmitted by resonant modes. Each resonant frequency corresponds to spatial modes having either odd or even values of $m + l$. The effective free spectral range for a cavity operating multi-mode, then, is just the spacing between “even” and “odd” peaks, i.e., $c/4L$. We therefore conclude that both the spatial coherence of the beam and its precise alignment along the axis of the cavity will have a critical effect on the instrument’s performance. In particular, if the beam is purely Gaussian and aligned precisely along the optic axis, the “odd” peaks disappear and the finesse is effectively doubled. I will show in section 1.6 that this finesse is the same as the parallel plane finesse to a very good approximation. Similarly, the finesse of the confocal cavity with multimode resonance is very close to half that of the parallel plane cavity.

1.5 Mode matching in a spherical cavity

In our simplified treatment of resonance in a parallel plane cavity we have ignored one important requirement for resonance, i.e., that the divergence of the beam must match the shape of the cavity walls. In particular, we assumed that the equiphase (or cophasal) surfaces of a given mode were planar. In the case of the spherical cavity, the equiphase surfaces of the allowed modes must match the spherical surfaces of the mirrors. (This fact is evident from the actual functions [3] that describe the modes, but I state it here as an intuitive prerequisite for coherent interference.) Mode matching also requires that the beam be aligned very precisely with the optic axis. Otherwise, the cavity will decompose a spatially coherent beam into higher-order modes since the asymmetry of the beam about the optic axis gives rise to non-zero values of l and m [1]. Two properties of a Gaussian beam that find relevance in the present discussion are the

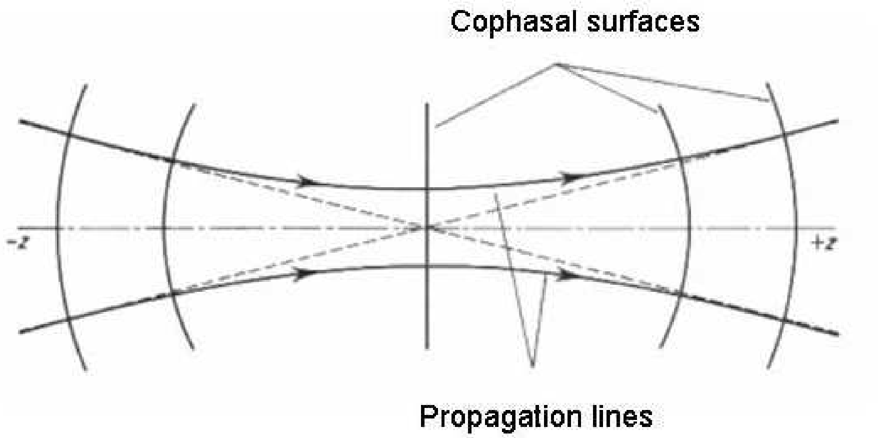

Fig. 5. Gaussian beam propagation in a confocal cavity. The beam waist is located in the center of the cavity, and the radius of curvature is matched to the curvature of the mirrors. Reproduced from [1].

spot size at the beam waist, denoted w_0 , and the complex beam parameter (or complex radius of curvature) *q*. As illustrated in Fig. 5, the beam waist must be located at the focus of the mirrors. It is here that the spot size is smallest, given [3] by

$$w_0 = \left(\frac{L\lambda}{2\pi}\right)^{\frac{1}{2}}. \tag{18}$$

The complex beam parameter *q(z)* at a point *z* from the beam waist is simply [3]

$$q(z) = q_0 + z \tag{19}$$

where

$$q_0 = iz_R. \tag{20}$$

The Rayleigh range z_R is the distance from the beam waist at which the spot size is increased by a factor of $\sqrt{2}$, and is given [3] by

$$z_R = \frac{\pi w_0{}^2}{\lambda} \tag{21}$$

An elegant formula called the *ABCD law of Gaussian beam propagation* can be used to determine the complex beam parameter at the output of an optical system given its value at the input. It states that the output parameter q_2 is given (in terms of the elements of the system's ABCD matrix) by

$$q_2 = \frac{Aq_1 + B}{Cq_1 + D}, \tag{22}$$

where q_1 is the input complex beam parameter. This law is used to determine the location of the beam waist and the spot size w_{02} at the beam waist after a thin lens. I refer the reader to [3] and Appendix C for the details of the derivation and simply cite the results here. The beam waist is located at a distance z_m from the lens defined by

$$z_m = \frac{f}{1 + (f/z_{R1})^2}. \tag{23}$$

If the Rayleigh range of the input beam $z_{R1} >> f$, then $z_M \cong f$, and the spot size at the waist is given by

$$w_{02} \cong \frac{\lambda f}{\pi w_{01}}, \tag{24}$$

where w_{01} is the spot size of the input beam. Optimal coupling of the Gaussian mode, therefore, may be accomplished in many cases by aperturing the beam to the appropriate spot size according to Eq. 24 and placing a lens at its focal length from the center of the cavity.

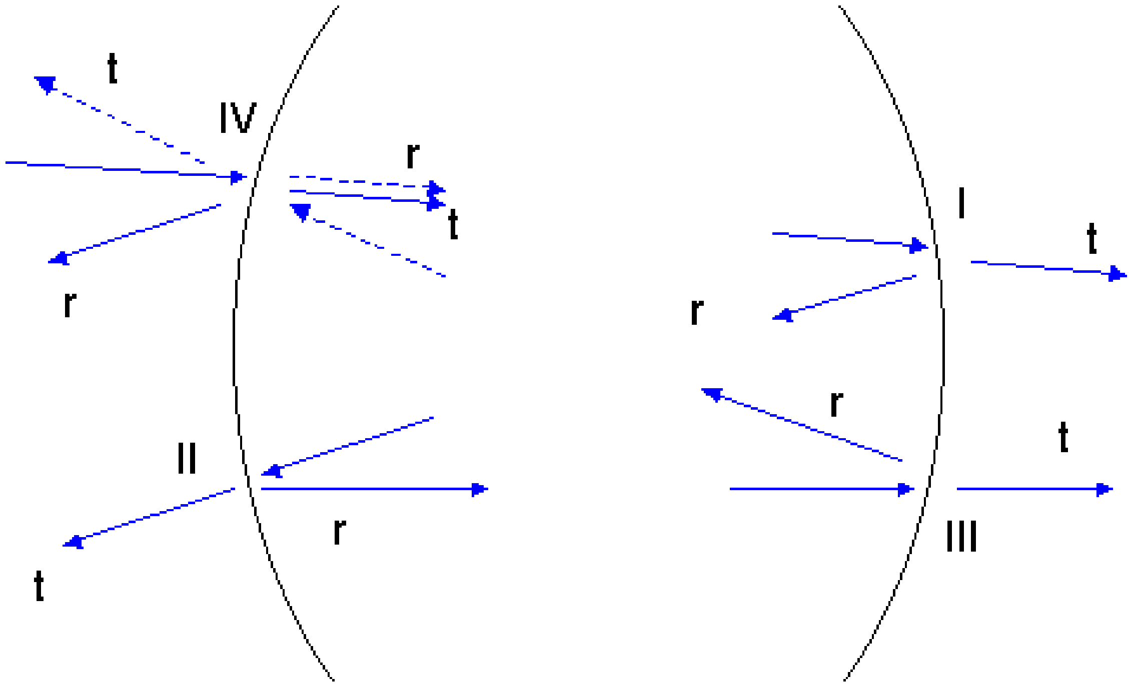

Fig. 6. Re-entrant rays in a confocal cavity. The dashed line indicates the second interaction at *IV*. At each reflection, the electric field amplitude is multiplied by *r*. The electric field transmitted at *I* is a superposition of all rays that exit after 4, 8, 12, . . . reflections. Adapted from [1].

1.6 Ray picture of the confocal cavity

As stated in the previous section, the confocal cavity breaks up an incoherent or misaligned beam into higher order modes that may then be thought of as propagating independently in the cavity. I demonstrated in section 1.4 that the degeneracy of higher order modes gives rise to transmission peaks that are spaced $c/4L$ apart, one-half the (true) free spectral range in the case of coherent light. The following discussion is intended to both illuminate this result and derive an expression for the finesse of a confocal cavity both for multi-mode and single mode operation. We will initially assume that the input is incoherent light, thus it may be applied in situations where a spatially coherent beam is either not mode matched or not precisely aligned with the optic axis. Later, we will examine the case of coherent input. For simplicity, the mirrors are assumed to have the same reflectance R and transmittance T, corresponding to the Fresnel coefficients r and t.

We consider a single ray as shown in Fig. 6, entering at a point *IV* at near-normal incidence. It is shown in Appendix A that the ABCD matrix corresponding to four successive reflections within the cavity is the identity matrix; a near-paraxial ray, therefore, retraces its path after four consecutive reflections. Such rays are said to be re-entrant. The electric field of the first beam to leave the cavity at point *I* may be expressed as

$$E_t^1 = T * E_i * \exp(i\alpha). \tag{25}$$

Every exit beam will have the same phase factor $\exp(i\alpha)$ associated with it, so from this point on we will let it be absorbed by the electric field E_i of the incident ray. The second beam to exit at I does so after four reflections, so its electric field is

$$E_t^{\ 2} = T * R^2 * E_i * \exp(i\phi), \tag{26}$$

where ϕ is the phase shift after one re-entrant path. In general, the mth beam exiting at I is given by

$$E_t^{\ m} = T * R^{2(m-1)} * \exp[(m-1)i\phi]. \tag{27}$$

Evaluating the infinite sum of all exit beams gives the electric field transmitted at I to be

$$E_t = E_i \frac{T}{1 - R^2 * \exp(i\phi)}. \tag{28}$$

After some algebra and a trigonometric substitution, it is shown in Appendix B that the transmission of the cavity T_c may be written as

$$T_c = \left|\frac{E_t}{E_i}\right|^2 = \frac{T_c \max}{1 + F \sin^2(\phi/2)} \tag{29}$$

where

$$T_c \max = \frac{T^2}{(1 - R^2)^2}, \tag{30}$$

$$F = \frac{4R^2}{(1 - R^2)^2}. \tag{31}$$

The finesse of the cavity, given by making the appropriate substitution for F in Eq. 5, is

$$\Im \cong \frac{\pi R}{1 - R^2}. \tag{32}$$

The reader is invited to compare these expressions with the corresponding results for the parallel plane cavity in section 1.3.

We can also derive the free spectral range by noting that the number of periods in a re-entrant path is double the result from the parallel plane case, viz.,

$$N_{con} = \frac{8\pi L}{\lambda}. \tag{33}$$

Modifying Eq. G accordingly leads to a free spectral range of $c/4L$ as shown in section 1.4 using mode theory.

Thus far, we have assumed incoherent light for the cavity input, but it is a simple matter to extend our results to the case of well-aligned coherent light by examining the interference that occurs between a ray entering at *I* and another ray entering at *II*, the diametrically opposite point. The following argument is based on the discussion provided in [1]. We first note that rays transmitted at (say) point *I* are of two types: (*a*) those originating from the ray entering at *IV*, and (*b*) those originating from the ray entering at *II*. The amplitudes and phase factors associated with type *a* rays have already been given. The reader may easily verify that the amplitude and phase factors of type *b* rays are $R\ \exp(i\phi/2)$, $R^3\ \exp(3i\phi/2)$, ... It follows that if the re-entrant path amounts to an even number of wavelengths, then constructive interference occurs. Conversely, odd numbers of wavelengths result in destructive interference. Coherence of the input beam, then, has two consequences. First, since the electric fields are doubled as compared with the incoherent case due to constructive interference, the intensity is quadrupled. Second, every other transmission peak disappears, effectively doubling the finesse. Hence,

$$\Im \cong \frac{2\pi R}{1-R^2} \tag{34}$$

for a precisely aligned coherent input beam. For commonly used mirror reflectivities this is, to a good approximation, equivalent to the finesse of the parallel plane cavity, though there appears to be no good analytical reason for this. (Fig. 7 shows the ratio of the single-mode confocal finesse to the plane finesse for reflectivities above 50%.) Additionally, it follows that the finesse in the case of incoherent light is about one-half of the finesse of the parallel plane cavity.

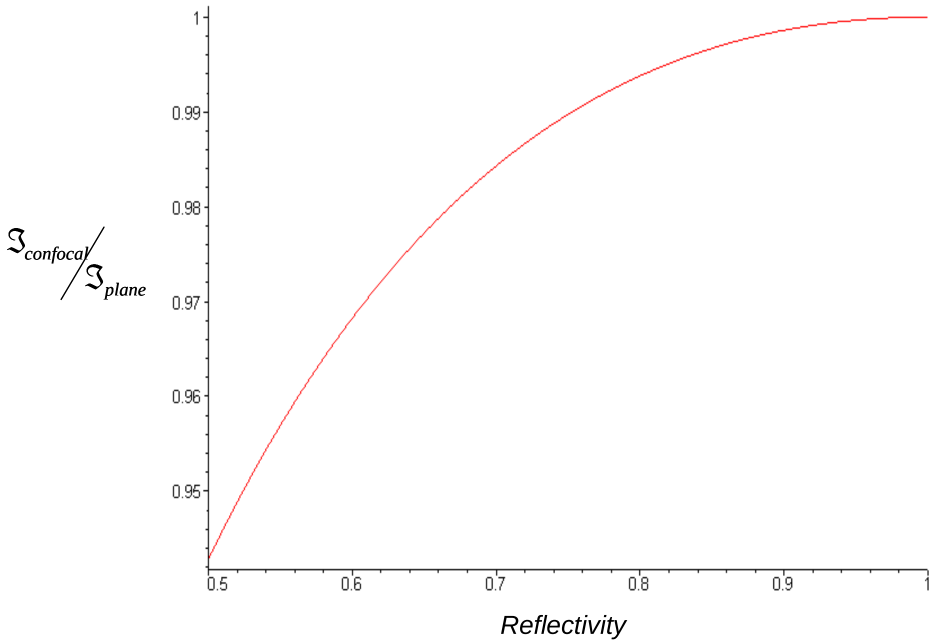

Fig. 7. Ratio of the confocal to the plane cavity finesse. The two are nearly equivalent, even for 50% reflectivity. As mirror reflectivity approaches 1, the two finesses approach exact equality.

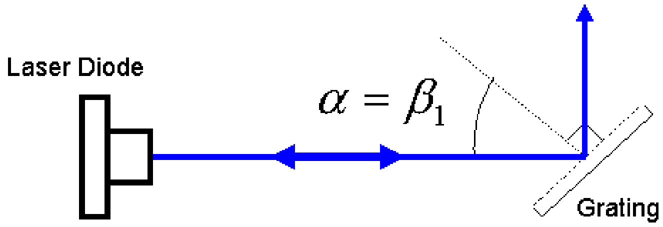

Fig. 8. Diffraction grating in Littrow configuration. The first-order beam is diffracted back into the diode for amplification of the selected wavelength.

Chapter II. EXPERIMENTAL SET-UP

In this chapter I will briefly describe the grating-stabilized extended cavity diode laser used to test the FP cavity. I also outline the procedures used to test mirror reflectance, assemble the interferometer, and align the beam.

2.1 Littrow external cavity

The Littrow cavity is perhaps the most common in use for tuning diode lasers because of its efficiency and simplicity. As shown in Fig. 8, the output of the diode strikes a high-quality planar diffraction grating. The grating is oriented so that the angle of incidence equals the angle of the first-order reflection from the normal. This is the condition for feedback into the laser diode.

For our purposes, we needed high resolution in the tuning frequency. The expression for the resolving power (defined to be ${}^{\lambda_0}\!/_{\Delta\lambda_{FWHM}}$) of a planar diffraction grating is given by $RP = mN$, where m is the diffraction order and N the number of lines illuminated. We used a 3600 l/mm grating 25mm in length (Richardson Grating

Laboratory, now Thermo RGL), giving us a maximum resolving power of $RP = 45000$. At 397nm, this gives a maximum resolution of 8.82 pm. This was sufficiently narrow in order to achieve the required linewidth; the laser diode operating single mode selects a single frequency of the external cavity that falls within a narrow gain envelope. A more detailed discussion on this topic is given in [5].

The wavelength of the feedback is extremely sensitive to the angle of incidence. The angular dispersion expresses the sensitivity of the feedback wavelength to the grating angle as

$$D = {}^{\partial\beta}\!\big/_{\partial\lambda}, \tag{35}$$

where $\partial\beta$ is the change in grating angle (or equivalently, the change in dispersion angle) and $\partial\lambda$ is the change in the feedback wavelength. In the Littrow cavity, the angular dispersion is given [6] to be

$$D = \frac{2}{\lambda}\tan\beta. \tag{36}$$

Assuming single frequency at 397nm and a grating angle of $45.6°$, the angular dispersion for our external cavity was 0.295 deg/nm. The translation per volt for the piezo-electric mount is (.061 + 1.5) μm [7], which corresponds to a shift $\Delta\lambda = 310$fm (or $\Delta\nu = 590$ MHz) per volt applied.

I placed the grating into a piezo-driven kinematic mirror mount (Thorlabs KCL-PZ) using a homemade adapter. Thorlabs gives the electro-mechanical angular resolution

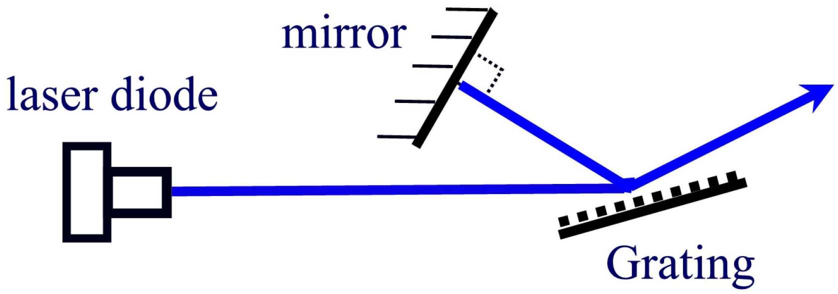

Fig. 9. The Littman-Metcalf external cavity. The condition for feedback requires that the first order beam strike the mirror at normal incidence. Its principal advantage is that the output beam does not change direction with tuning. Tuning is accomplished by changing the mirror angle slightly.

of this mount to be 0.06 Arc Sec or $16.7\mathrm{E}-6°$, corresponding to a frequency resolution of 110MHz. For both stability and convenience in moving the set-up when necessary, cage mounting was employed to attach the grating assembly to the diode mount. For further stability, the cage was also bolted to the bench. Details of diode laser operation in the Littrow cavity, including a photograph of the mounting hardware, is provided in [5].

2.2 Littman-Metcalf External Cavity

I was able to obtain a clean signal using the Littrow cavity, but another design of special interest is the Littman-Metcalf configuration, shown in Fig. 9. Though I was unable to achieve single-frequency operation using the Littman-Metcalf cavity, it is nevertheless worth discussing here because it is often preferred. Its main advantage over the Littrow configuration is that the output beam does not change direction as the laser is tuned, but this convenience is paid for in the form of lost power. In the Littman-Metcalf configuration, the beam impinges on the grating at grazing angle. The first-order (m = 1) diffracted beam is directed at normal incidence onto a mirror that reflects the beam back

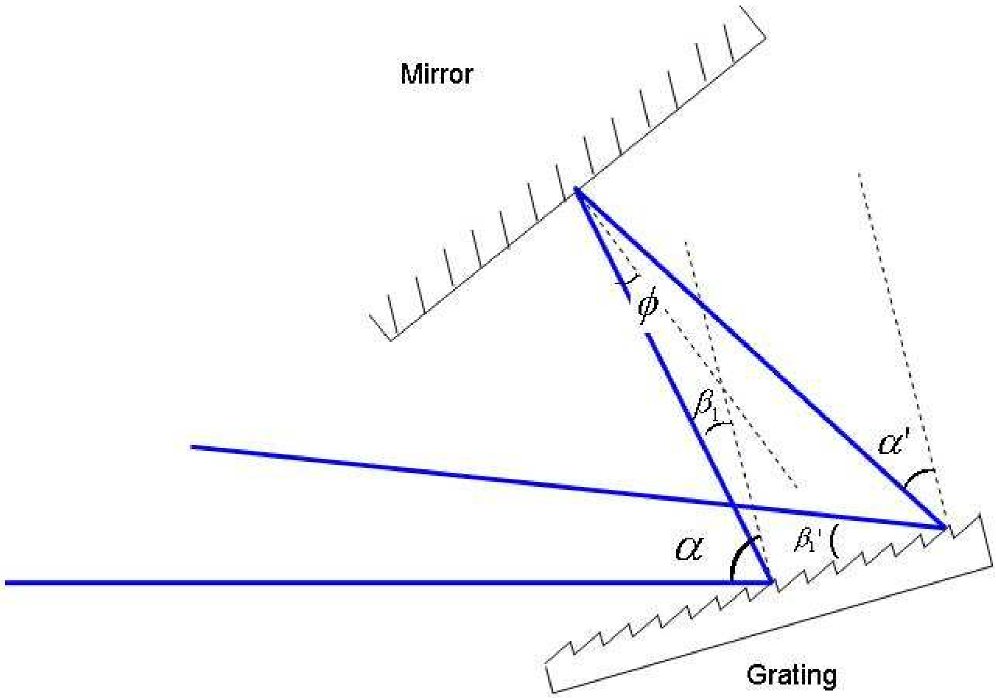

Fig. 10. Alignment in Littman-Metcalf configuration. The angle ϕ must be zero in order that $\alpha = \beta_1'$. Adapted from [8].

onto the grating. The grating breaks up the beam again into a reflected beam and one or more higher-order beams. The first-order reflection of this beam ($m' = 1$) is redirected towards the diode. Tuning of the laser is accomplished by changing the angle of the mirror slightly.

The necessity of directing the beam to the mirror at normal incidence is derived from the equations for both first-order reflections off the grating, i.e.,

$$\begin{aligned} \lambda &= x(\sin\alpha + \sin\beta_1), \\ \lambda &= x(\sin\alpha' + \sin\beta_1'), \end{aligned} \tag{37}$$

where x is the line spacing and angles are as shown in Fig. 10. (The subscript indicates that the beam involved is first order.) Feedback requires that $\alpha = \beta_1' = \theta_0$, and Eqs. 37 become

$$\begin{aligned} \lambda/x &= (\sin\theta_0 + \sin\beta_1), \\ \lambda/x &= (\sin\alpha' + \sin\theta_0). \end{aligned} \tag{38}$$

By inspection, the solution to this system must be $\alpha' = \beta_1$. It follows that the mirror is positioned perpendicular to the beam. The Littman-Metcalf cavity using only first-order reflections is described by the single equation

$$\lambda/x = (\sin\theta_0 + \sin\beta_1). \tag{39}$$

As mentioned, the Littman-Metcalf configuration leads to more power loss as compared to the Littrow cavity. In the Littrow cavity, the first-order reflection is sent directly into the laser diode; the Littman-Metcalf cavity throws away most of the first order reflection by sending it to the grating a second time.

2.3 Fabry-Perot construction

2.3.1 Aluminum deposition onto lenses

I deposited aluminum coatings onto several microscope slides using a thermal evaporator. The coatings invariably exhibited irregularities that gave rise to inconsistencies in their reflectance and caused scattering. These flaws in the coatings were evidently due to residues of oil or water on the slides prior to deposition. Because the degree of cleanliness necessary to avoid these blemishes cannot be accomplished using standard optic cleaning techniques, the final coatings were deposited by MOXTEK, Inc., a firm based in Orem, UT specializing in thin films. The process of cleaning the lenses included agitating them in soapy water, bathing them in sulfuric acid to remove organic matter, etching the surfaces to be coated, and baking out residual water [9].

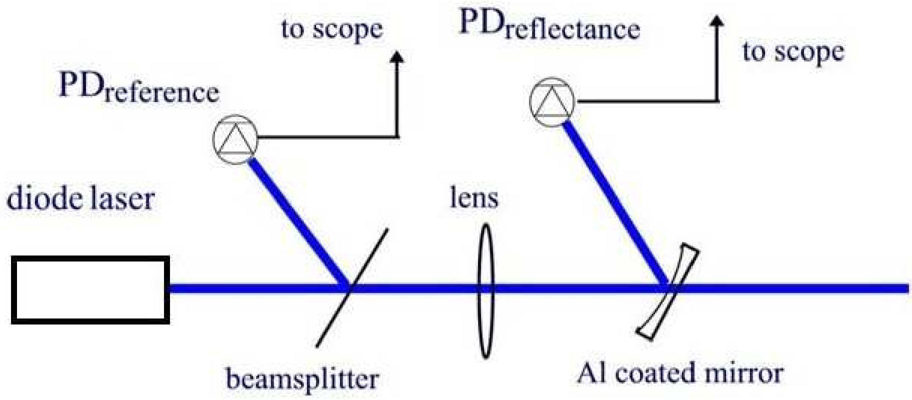

Fig. 11. Set-up for measuring mirror reflectivity.

2.3.2 Reflectance measurements

I verified that the reflectivities of the mirrors were equally matched at a value near the desired 70%. The set-up for making these measurements is shown in Fig. 11. A beamsplitter picks off part of the output of the diode laser and $PD_{reference}$ measures its relative intensity for use as a reference. (This was necessary to account for variations in the laser's output intensity due to mode hops.) The mirror to be studied was placed about $20°$ from normal to the beam, and $PD_{reflectance}$ was placed a short distance from the mirror to measure the relative reflected intensity. A lens was used to defocus the beam to a desirable spot size (about 2mm) onto $PD_{reflectance}$. A digital oscilloscope read the output of both photodiodes simultaneously, hence the measurement of $PD_{reflectance}$ could be easily normalized using the reference measurement. I then measured the intensity of the full beam after the beam splitter with $PD_{reflectance}$, also normalized by the output of $PD_{reference}$. The reflectance could then be calculated as the ratio of the two (normalized) measurements. Six reflectance measurements were made for each mirror.

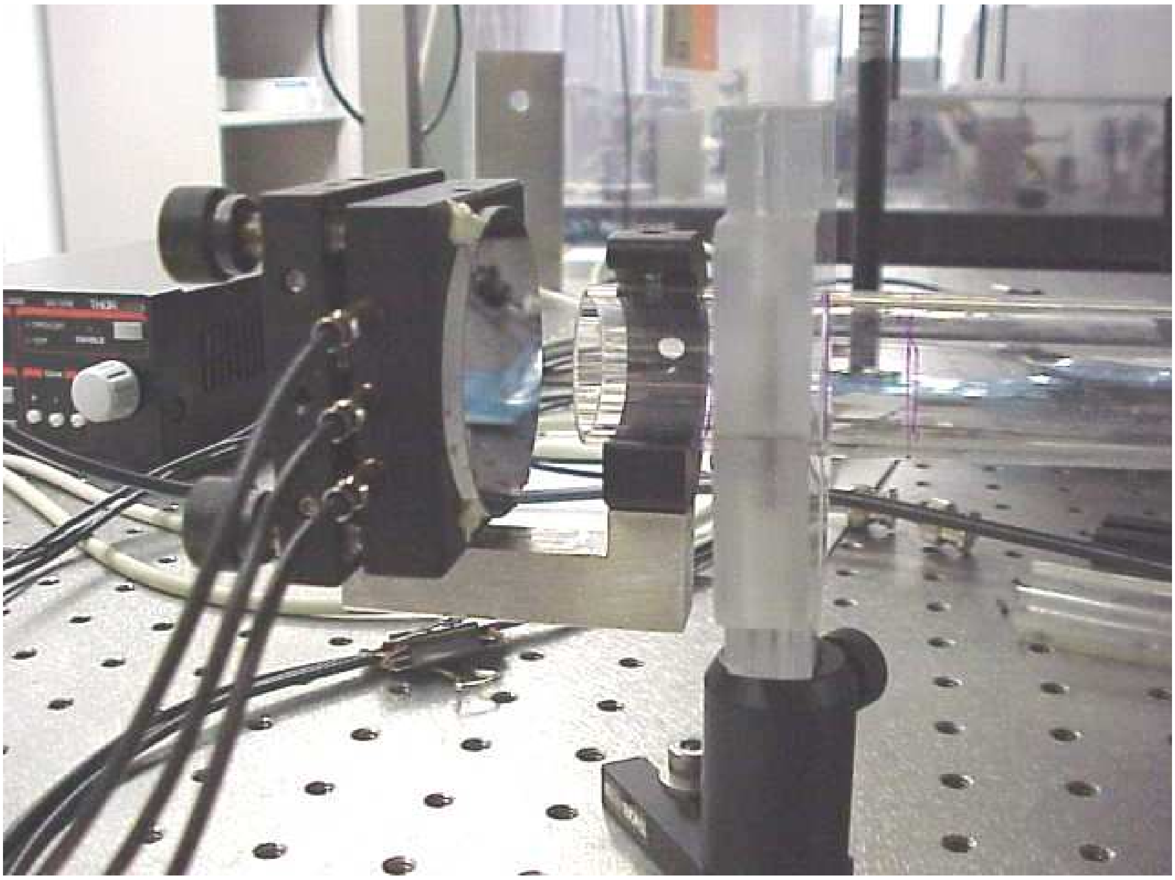

Fig. 12. One end of the Fabry-Perot cavity.

2.3.3 Assembling the Apparatus

The Fabry-Perot cavity that I constructed consists of two aluminum coated plano-concave lenses with f = 1000mm and radius of curvature 516mm (Coherent 43-2104) separated by a 1” diameter quartz tube. The mirrors were originally spaced a distance of 80cm apart, but later the tube was cut to make place the mirrors at confocal separation.

Fig. 12 shows one end of the apparatus. Both mirrors are fastened to the front plate of a Thorlabs kinematic mirror mount with small dabs of epoxy patch applied to the edges each mirror. For the purpose of scanning the mirror separation, the input mirror is fastened to a piezo-electric mirror mount (Thorlabs KC1-PM). The mounts are fastened to the ends of the quartz tube using a homemade arm and a post clamp. A two-piece, homemade Plexiglas jaw is employed near each end of the tube to mount the cavity to the bench.

2.3.4 Set-up and alignment

I tested the cavity in two experiments. For the first experiment the cavity was nonconfocal, with a mirror separation L = 80cm. Additionally, the input used was an infrared beam known to be stable at a single-frequency. The profile of this beam was also observed to be Gaussian. A lens was placed in the beam with its focus at the center of the cavity, and an iris was used to aperture the beam according to Eq. 24 to a diameter of 0.6 ± 0.2 mm. The input frequency was ramped, and the transmitted intensity was measured with a photodiode.

The second experiment was performed in similar fashion using a 397nm input beam from the GaN diode laser in the Littrow configuration. The profile of the beam was observed to contain higher order spatial modes, particularly the TEM_{10} mode. The cavity for this experiment was confocal, with a mirror separation of 516mm. The set-up is shown in Fig. 13. I aligned the beam along the axis of the Fabry-Perot cavity using two flat mirrors. The beam was apertured to a diameter of $0.7 \pm .2$ mm and an $f = 500\,\text{mm}$ lens was placed a focal length away from the center of the cavity. Initially, the lens was aligned so that the beam was reflected back through the aperture. The resulting feedback sabotaged the laser operation, and the lens was afterward intentionally misaligned slightly to minimize this problem.

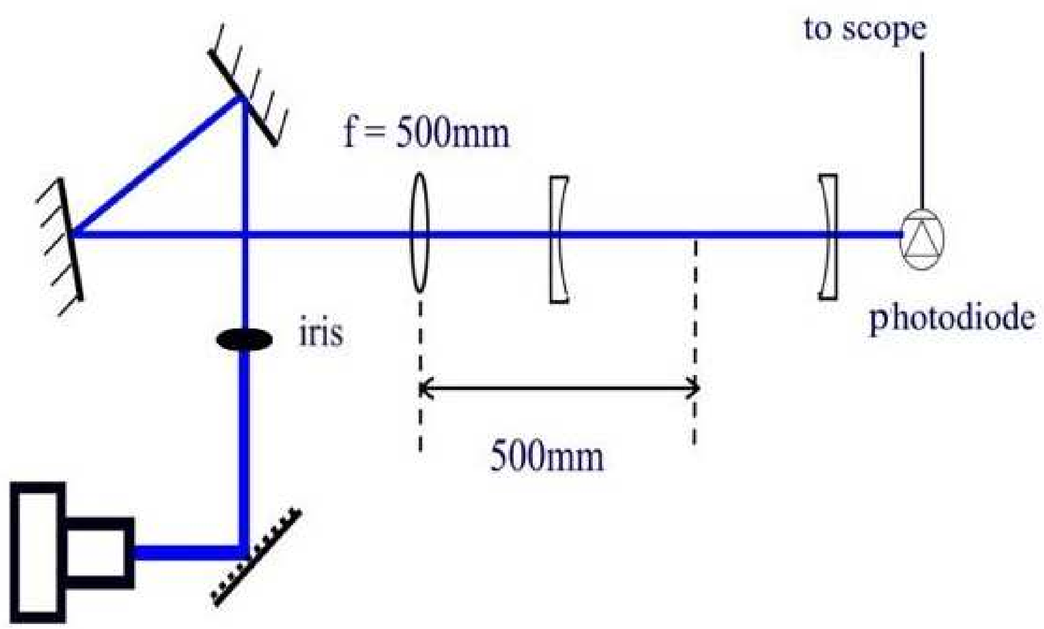

Fig. 13. Experimental set-up used to test the Fabry-Perot cavity.

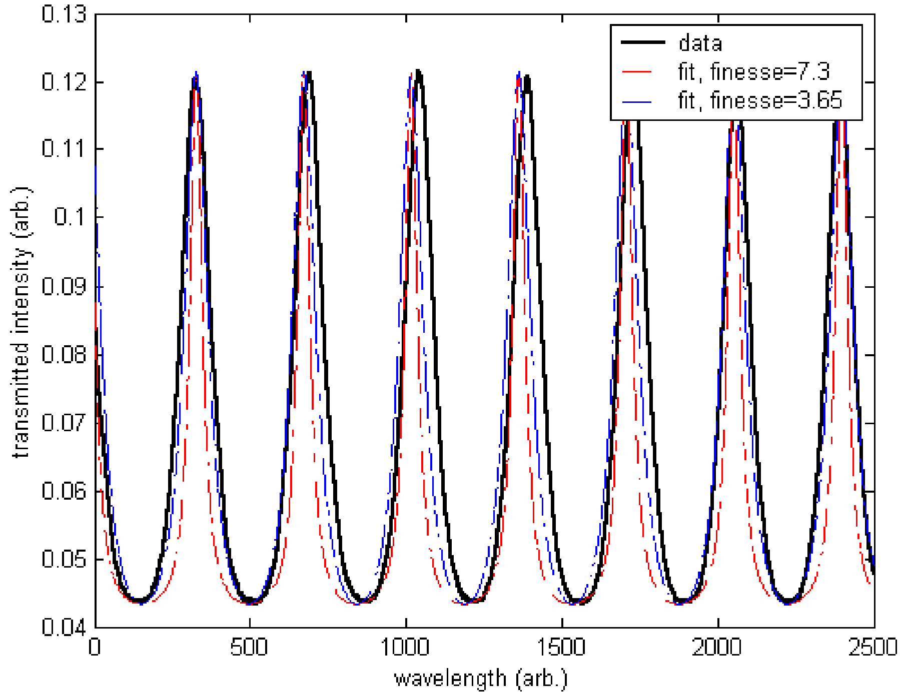

Fig. 14. Transmission of the nonconfocal cavity with mirror separation of 80cm and infrared input compared with predicted signals for coherent and incoherent input. The larger finesse corresponds to coherent input.

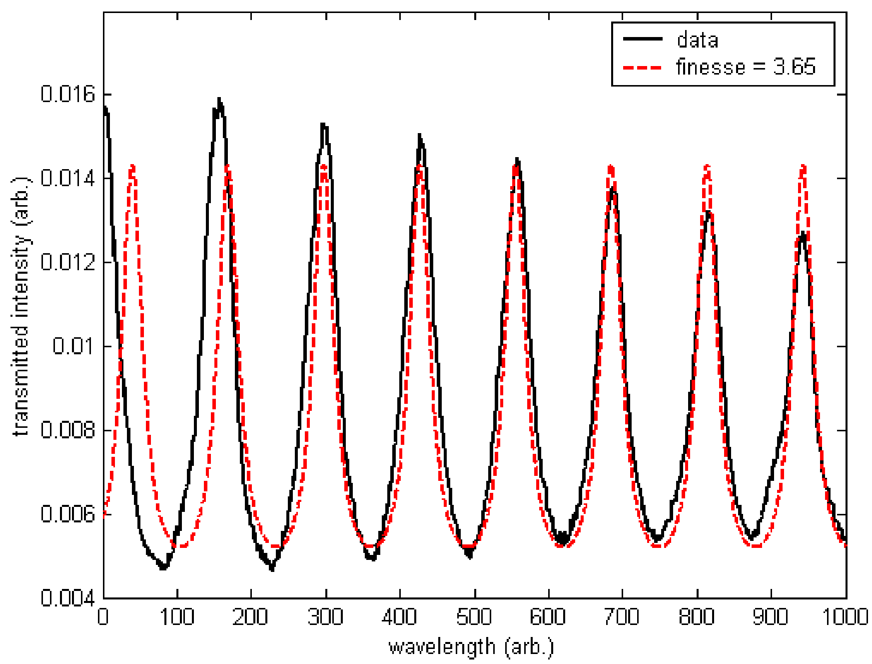

Fig. 15. Comparison of confocal cavity transmission with the signal expected for spatial incoherence and/or off-axis propagation

Chapter III. Results

3.1 Presentation of Results

The mirror reflectivities were measured to be 66$\pm$ 1% and 66 $\pm$ 2%. This corresponds to a finesse coefficient of F = 5.4 $\pm$ 0.25 and a finesse of $\Im$ = 3.65 $\pm$ 0.15 in the case of incoherent input in the confocal cavity.

The transmitted intensity of the nonconfocal (L = 80cm) cavity is shown in Fig. 14. The peaks on either side match well with the signal predicted for a confocal cavity with incoherent input, but the signal in the center region of the plot is out of phase with this prediction. We conclude that the period does not remain constant, but its average is the same as the period predicted for incoherent input. The peak widths themselves match the incoherent prediction fairly well, but they are slightly larger.

The output of the confocal cavity with blue laser input also matched more closely with the signal predicted for multimode resonance than for single mode, but had deviations from the prediction similar to those observed in the output of the nonconfocal cavity. Fig. 15 shows that the transmission peaks were slightly wider compared to the prediction, but the most striking characteristic of the signal is the attenuation of the peak amplitudes. This effect was certainly not caused by the Fabry-Perot, but is related to the intensity of the diode laser itself, probably caused by the shifting of the external cavity mode away from resonance in the diode. It is useful to incorporate this effect into the theoretical prediction in order to more clearly compare it with the experimental result. Fig. 16 shows unambiguously that the peaks are indeed slightly broadened compared to

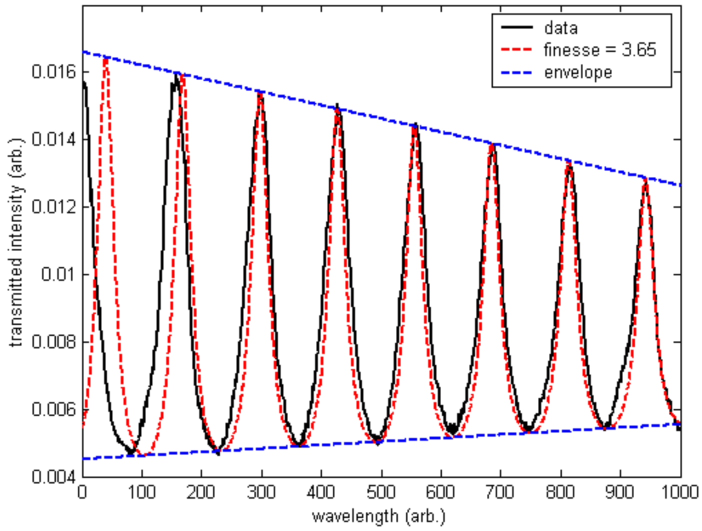

Fig. 16. Transmission of the confocal cavity compared to the transmission predicted when taking the attenuation into account.

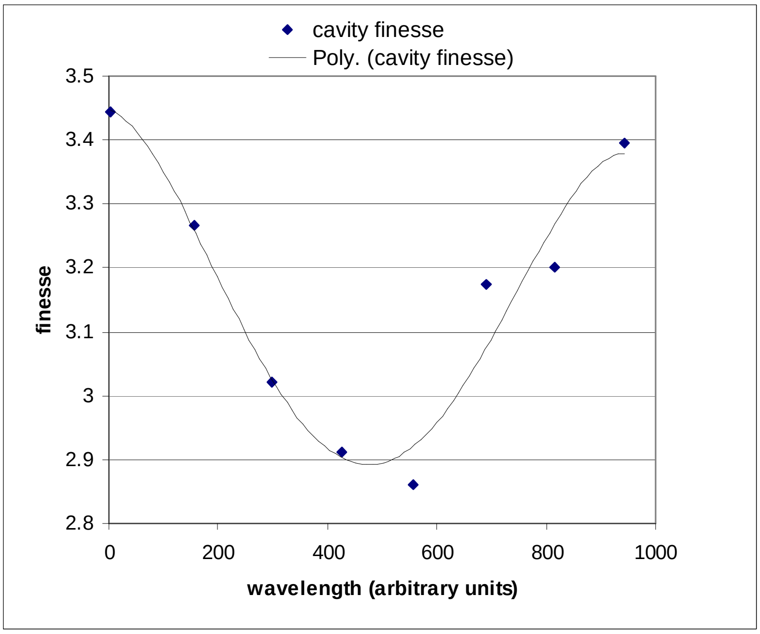

Fig. 17. Measured cavity finesse vs. wavelength. The trendline, a 4^{th} order polynomial fit generated in Microsoft Excel, was used to generate the variable finesse fit for the transmission shown in Fig. 16.

the predicted output of a cavity operating multimode. Fig. 17 shows that the measured finesse of the cavity, determined by measuring the width and period associated with each individual peak, varies as a function of wavelength. (This does not mean that the actual finesse varies, but that the measurement of the finesse differs depending on which peak is used.) The mean measurement of the finesse is 3.2 ± 0.2, a significant variation from the expected value based on reflectivity measurements.

A careful inspection of the left side of Fig. 16 reveals another important feature; the period appears to be significantly larger in this region. To more closely examine the effect of period variations on the transmission, it is illuminating to compare the output of the cavity with a plot whose finesse varies according to the trendline shown in Fig. 16. In Fig. 18 (on the following page), as in all previous plots of the predicted transmission, the period is assumed to be constant, so the finesse is varied in the fit only by changing the peak width. Thus, any deviations from the prediction should be attributed to variations in the period. As may have been suspected, the period is indeed much larger near the left side of the plot, while it is more or less constant everywhere else. Such variations in the period may be reasonably attributed to non-linear expansion of the piezo crystals with applied voltage.

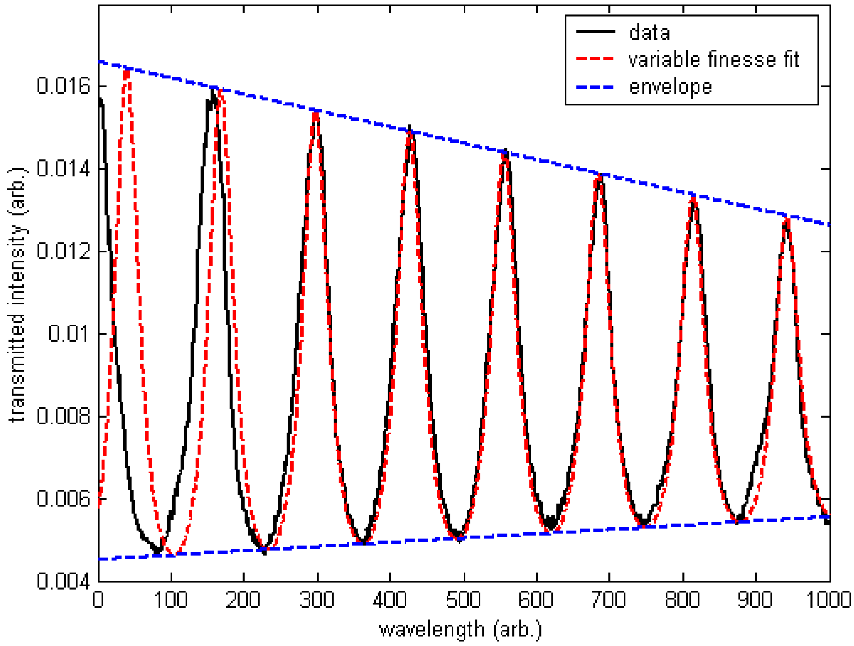

Fig. 18. Comparison of FP transmission with a fit having finesse that varies according to the trendline shown in Fig. 17 and bound by the envelope shown. The fit assumes that the period is constant and that changes in the measurements of finesse are due entirely to changes in peak width. This appears to be a reasonable assumption everywhere except at the first two peaks, where the increased period is obviously responsible for the higher finesse.

3.2 Discussion and conclusions

Though the cavity may be used in multi-mode operation, single-mode operation is preferred. The most probable causes for of multi-mode resonance are improper mode matching and misalignment of the beam. I first examine the possibility of improper coupling of the Gaussian mode to the cavity.

Careful examination of Eq. 24 reveals that it is not a valid criterion for mode matching in this case. The assumption implicit in Eq. 24 that $z_{R1} >> f$ does not hold true; in fact, the Rayleigh range calculated for the beam is $z_{R1} \cong f$. The calculation in Appendix C also shows that the appropriate distance of the lens from the confocal point should have been 25cm, an impossible distance for a cavity that is only 516mm long. I conclude that a lens of longer focal length is required for proper mode matching. I was unable to check these conclusions experimentally, however. The diode laser operated single mode for a short time, allowing me to obtain the results presented here, but afterward I was unable to restore it to single-mode operation.

It is also possible that the beam alignment along the optical axis was not sufficiently precise. Viewing the transmitted intensity pattern with a CCD camera would facilitate precise alignment and help to ensure that only the Gaussian mode is allowed to resonate in the cavity.

References

[1] J M Vaughan, *The Fabry-Perot Interferometer: History, Theory, Practice and Applications*, 1st ed. (Philadelphia, Pennsylvania, 1989), pp. 184-205.

[2] Justin Peatross, *Physics of Light and Optics*, 1st ed. http://optics.byu.edu/BYUOpticsTextbook.htm, pp. 101-119, 197.

[3] Orazio Svelto, *Principles of Lasers*, 3rd ed. (Plenum Press, New York, 1989), pp. 17, 162-181.

[4] Taken from http://electron9.phys.utk.edu/optics421/modules/m7/lasers.htm. 2002.

[5] D. Farrell, "Single-Frequency 397nm Diode Laser for Ca^+ Spectroscopy," Senior Thesis (Brigham Young University, Provo, UT, 2001).

[6] Christopher Palmer, *Diffraction Grating Handbook*, 5th ed. http://www.gratinglab.com/library/handbook5.

[7] M. Amissah, Thorlabs Corp. (private communication).

[8] Michael G. Littman and Harold J. Metcalf, "Spectrally narrow pulsed dye laser without beam expander," *Appl. Opt.* **17,** 2224 (1978).

[9] R. Perkins, MOXTEK, Inc. (private communication).

Appendix A: The ABCD matrix for the confocal cavity

This computation shows that the *ABCD* matrix corresponding to four reflections in the confocal cavity is the identity matrix.

```
> restart:with(linalg):
Warning, the protected names norm and trace have been
redefined and unprotected
```

For the confocal cavity,

```
> L:=R;
```

$$L := R$$

The matrix for (length + reflection + length) is (see [1])

```
> ABCD:=Matrix([[1-2*L/R, 2*L-2*L^2/R], [-2/R, 1-2*L/R]]);
```

$$ABCD := \begin{bmatrix} -1 & 0 \\ -2\,\frac{1}{R} & -1 \end{bmatrix}$$

The matrix for a single reflection is

```
> ref:=Matrix([[1, 0], [-2/R, 1]]);
```

$$ref := \begin{bmatrix} 1 & 0 \\ -2\,\frac{1}{R} & 1 \end{bmatrix}$$

The total matrix for a round trip [(L + ref + L) + ref + (L + ref + L) + ref] is

```
> ABCDtot:=multiply(ref,ABCD,ref,ABCD);
```

$$ABCDtot := \begin{bmatrix} 1 & 0 \\ 0 & 1 \end{bmatrix}$$

Appendix B: Derivation of finesse for the confocal cavity

This computation derives the finesse of a confocal cavity operating multimode given in Eqs. 29 - 31.

```
> restart:
> Et:=Ei*T*Sum((R)^(2*m-2)*exp((m-1)*I*phi),m=1..infinity);
```

$$Et := \mathrm{Ei}\ T\left(\sum_{m=1}^{\infty} R^{(2\,m-2)}\,\mathbf{e}^{((m-1)\,\phi\,I)}\right)$$

```
> E:=Ei*T*sum((R)^(2*m-2)*exp((m-1)*I*phi),m=1..infinity);
```

$$E := -\frac{\mathrm{Ei}\,T}{R^2\,\mathbf{e}^{(\phi\,I)} - 1}$$

```
> Estar:= Ei*T/(1-R^2*exp(-I*phi));
```

$$Estar := \frac{\mathrm{Ei}\,T}{1 - R^2\,\mathbf{e}^{(-I\,\phi)}}$$

The intensity is $|Et|^2$

```
> Etsrd:=E*Estar;
```

$$Etsrd := -\frac{\mathrm{Ei}^2\,T^2}{(R^2\,\mathbf{e}^{(\phi\,I)} - 1)\,(1 - R^2\,\mathbf{e}^{(-I\,\phi)})}$$

```
> den:=expand(denom(Etsrd));
```

$$den := -R^2\,\mathbf{e}^{(\phi\,I)} + R^4 + 1 - \frac{R^2}{\mathbf{e}^{(\phi\,I)}}$$

```
> den:=simplify(%);
```

$$den := -2\,R^2\cos(\phi) + R^4 + 1$$

```
> den:=subs(cos(phi)=1-2*sin(phi/2)^2,den);
```

$$den := -2\,R^2\left(1 - 2\sin\left(\frac{\phi}{2}\right)^2\right) + R^4 + 1$$

```
> den:=1+R^4-2*R^2+4*R^2*sin(phi/2)^2;
```

$$den := 1 + R^4 - 2\,R^2 + 4\,R^2\sin\left(\frac{\phi}{2}\right)^2$$

This simplifies to

```
> den:=(1-R^2)^2+4*R^2*sin(1/2*phi)^2;
```

$$den := (1 - R^2)^2 + 4\,R^2\sin\left(\frac{\phi}{2}\right)^2$$

```
> Etsrd:=numer(Etsrd)/den;
```

$$Etsrd := \frac{\mathrm{Ei}^2\,T^2}{(1 - R^2)^2 + 4\,R^2\sin\left(\frac{\phi}{2}\right)^2}$$

The fraction of light transmitted from the cavity Tc is $Tc = \frac{|Et|^2}{|\mathrm{Ei}^2|}$:

```
> Tc:=Etsrd/Ei^2;
```

$$Tc := \frac{T^2}{(1-R^2)^2 + 4 R^2 \sin\left(\frac{\phi}{2}\right)^2}$$

Dividing the numerator and denominator by $(1-R^2)^2$, Eqs. 29-31 are obtained.

Appendix C: Matching the Gaussian mode to the confocal cavity

This will determine the distance the f = 500mm lens should be from the first mirror.

```
> restart:with(linalg):assume(z,real);assume(f,real);assume(Zr1,real);assume(lambda,real);assume(w01,real);
```

```
Warning, the protected names norm and trace have been redefined and unprotected
```

Note that I plugged in the numbers for λ, *L*, and *f* at this point in order to get the numerical solutions, but ran the code again without these substitutions up to the expression for *z*. This was done to show the expression for *z* symbolically.

```
> lambda:=397e-9;L:=.516;f:=.5;
```

$$\lambda := .397\ 10^{-6}$$

$$L := .516$$

$$f := .5$$

```
> ABCD:=<<1-z/f | z> , <-1/f | 1>>;
```

$$ABCD := \begin{bmatrix} 1 - \frac{z\sim}{f\sim} & z\sim \\ -\frac{1}{f\sim} & 1 \end{bmatrix}$$

Assume the waist is located at the lens, and that its spot size there is *w01*.

```
> A:=ABCD[1,1];
```

```
B:=ABCD[1,2];
C:=ABCD[2,1];
Di:=ABCD[2,2];
```

$$A := 1 - \frac{z\sim}{f\sim}$$

$$B := z\sim$$

$$C := -\frac{1}{f\sim}$$

$$Di := 1$$

```
> Zr1:=Pi*w01^2/lambda;
```

$$Zr1 := \frac{\pi\, w01\sim^2}{\lambda\sim}$$

w01 is the spot size at the lens.

The complex beam parameter at the lens is

```
> q1:=I*Zr1;
```

$$q1 := \frac{I\, \pi\, w01\sim^2}{\lambda\sim}$$

By the *ABCD* Law, the *q2* may be inverted as

```
> q2inv:=(C+Di*(1/q1))/(A+B*(1/q1));
```

$$q2inv := \frac{-\frac{1}{f\sim} - \frac{I\, \lambda\sim}{\pi\, w01\sim^2}}{1 - \frac{z\sim}{f\sim} - \frac{I\, z\sim\, \lambda\sim}{\pi\, w01\sim^2}}$$

Now we work with *q2inv* so we can pick off the real and imaginary parts. Maple can't separate them by itself using the "Re" and "Im" commands, so we have to help it. First we rationalize so that the denominator is real, then pick off the real part of the numerator.

```
> q2inv:=rationalize(%);
```

$$q2inv := \frac{(\pi\, w01\sim^2 + I\, \lambda\sim\, f\sim)\,(-f\sim\, \pi\, w01\sim^2 + z\sim\, \pi\, w01\sim^2 - I\, z\sim\, \lambda\sim\, f\sim)}{f\sim^2\, \pi^2\, w01\sim^4 - 2\, f\sim\, \pi^2\, w01\sim^4\, z\sim + z\sim^2\, \pi^2\, w01\sim^4 + z\sim^2\, \lambda\sim^2\, f\sim^2}$$

```
> num:=numer(%);
```

$$num := (\pi\, w01\sim^2 + I\,\lambda\sim f\sim)\,(-f\sim \pi\, w01\sim^2 + z\sim \pi\, w01\sim^2 - I\, z\sim \lambda\sim f\sim)$$

```
> expand(%);
```

$$-\pi^2\, w01\sim^4 f\sim + \pi^2\, w01\sim^4 z\sim - I\,\lambda\sim f\sim^2 \pi\, w01\sim^2 + \lambda\sim^2 f\sim^2 z\sim$$

```
> Rnum:=Re(%);
```

$$Rnum := -\pi^2\, w01\sim^4 f\sim + \pi^2\, w01\sim^4 z\sim + \lambda\sim^2 f\sim^2 z\sim$$

Now we can get the real and imaginary parts of *q2inv*:

```
>  Real:=Rnum/denom(q2inv);
```

$$Real := \frac{-\pi^2\, w01\sim^4 f\sim + \pi^2\, w01\sim^4 z\sim + \lambda\sim^2 f\sim^2 z\sim}{f\sim^2 \pi^2\, w01\sim^4 - 2\, f\sim \pi^2\, w01\sim^4 z\sim + z\sim^2 \pi^2\, w01\sim^4 + z\sim^2 \lambda\sim^2 f\sim^2}$$

```
> Imag:=Im(num)/denom(q2inv);
```

$$Imag := -\frac{\lambda\sim f\sim^2 \pi\, w01\sim^2}{f\sim^2 \pi^2\, w01\sim^4 - 2\, f\sim \pi^2\, w01\sim^4 z\sim + z\sim^2 \pi^2\, w01\sim^4 + z\sim^2 \lambda\sim^2 f\sim^2}$$

The beam waist is located where the real part of *q2* is infinite, or where the real part of *q2inv* vanishes. (The radius of curvature is ∞.)

```
> z:=solve(Real=0,z);
```

$$z := \frac{\pi^2\, w01\sim^4 f\sim}{\pi^2\, w01\sim^4 + \lambda\sim^2 f\sim^2}$$

This expression simplifies to Eq. 23:

```
> z:=f/(1+(f/Zr1)^2);
```

$$z := \frac{f\sim}{1 + \frac{f\sim^2 \lambda\sim^2}{\pi^2\, w01\sim^4}}$$

```
> Zr1:=evalf(Zr1);
```

$$Zr1 := .7913331623\ 10^{7}\ w01\sim^{2}$$

The parameter q may also be given by $\frac{1}{q} = \frac{1}{R} - \frac{i\,\lambda}{\pi\,w^2}$. We now can solve for the spot size at the lens by setting the imaginary part of *q2inv* equal to $-\frac{\lambda}{\pi\,w02^2}$. But Maple needs some help to make sure "Imag" is a function only of w01. Again, the "subs" command is ineffective if the variable name *Imag* is used, so I give it the expression explicitly.

```
> Imag:=subs(z=.5*1/(1+.3940224999e-13/(Pi^2*w01^4)),-
.3969999999e-6*Pi*w01^2/(Pi^2*w01^4-
4.*Pi^2*w01^4*z+4.*z^2*Pi^2*w01^4+.1576089999e-12*z^2));
```

$$Imag := -.3969999999\ 10^{-6}\ \pi\ w01\sim^{2} \Bigg/ \left(\pi^2\ w01\sim^{4} - \frac{2.0\ \pi^2\ w01\sim^{4}}{1 + \frac{.3940224999\ 10^{-13}}{\pi^2\ w01\sim^{4}}} + \frac{1.00\ \pi^2\ w01\sim^{4}}{\left(1 + \frac{.3940224999\ 10^{-13}}{\pi^2\ w01\sim^{4}}\right)^2} + \frac{.3940224998\ 10^{-13}}{\left(1 + \frac{.3940224999\ 10^{-13}}{\pi^2\ w01\sim^{4}}\right)^2} \right)$$

The spot size at the beam waist in the cavity is given in Eq. 18 to be

```
> w02:=evalf((L*lambda/(2*Pi))^(1/2));
```

$$w02 := .0001805635854$$

Finally, we solve for the spot size *w01* at the lens:

```
> w01:=solve(Imag=-lambda/(Pi*w02^2),w01);
```

$$w01 := -.0002494091168 - .00003129863967\,I,\ -.0002494091168 + .00003129863967\,I,$$
$$-.0001777421059 - .0001777421059\,I,\ -.0001777421059 + .0001777421059\,I,$$
$$.0001777421059 - .0001777421059\,I,\ .0001777421059 + .0001777421059\,I,$$
$$.0002494091168 - .00003129863967\,I,\ .0002494091168 + .00003129863967\,I$$

The answer that makes the most sense is .00025, because it is positive and the imaginary part is very small. Now we can solve for the distance *z* from the lens to the confocal point.

```
> w01:=.00025;
```

$$w01 := .00025$$

```
> evalf(z);
```

$$.5\,\frac{1}{1. + \frac{.3992282605\ 10^{-14}}{w01\sim^4}}$$

Again, the substitution must be done explicitly.

```
> z:=subs(w01=.00025,.5*1/(1+.3940224999e-13/(Pi^2*w01^4)));
```

$$z := .5\,\frac{1}{1 + \frac{10.08697600}{\pi^2}}$$

```
> evalf(z);
```

$$.2472769434$$

We can now get the Rayleigh range for free:

```
> Zr1:=subs(w01=.00025,7913331.623*w01^2);
```

$$Zr1 := .4945832264$$

We conclude that the Gaussian mode cannot be matched to the cavity using an *f*=500mm lens, since a distance *z* = 25cm from the confocal point does not lie outside the cavity. Note that the Rayleigh range is about the same as the focal length, which is why Eq. 24 was invalid.

Try a lens with a longer focal length.

```
>
restart:with(linalg):assume(z,real);assume(f,real);assume(Z
r1,real);assume(lambda,real);assume(w01,real);
```

```
Warning, the protected names norm and trace have been
redefined and unprotected
```

```
> lambda:=397e-9:L:=.516:f:=.75:
```

```
> ABCD:=<<1-z/f | z> , <-1/f | 1>>:
> A:=ABCD[1,1]:
B:=ABCD[1,2]:
C:=ABCD[2,1]:
Di:=ABCD[2,2]:
```

```
>  Zr1:=Pi*w01^2/lambda:
```

```
> q1:=I*Zr1:
```

Apply the *ABCD* law:

```
> q2inv:=(C+Di*(1/q1))/(A+B*(1/q1)):
```

This time we only need to worry about getting the imaginary part, since we have already shown that Eq. 23 gives the correct distance *z* of the beam waist from the lens.

```
> q2inv:=rationalize(%):
```

```
> num:=numer(%);
```

$$num := (1.333333333\ \pi\ w01\sim^2 + .3969999999\ 10^{-6}\ I)$$
$$(-1.\ \pi\ w01\sim^2 + 1.333333333\ z\sim\ \pi\ w01\sim^2 - .3969999999\ 10^{-6}\ I\ z\sim)$$

```
> num:=expand(%):
```

```
> Imag:=Im(num)/denom(q2inv);
```

$$Imag := -.3969999999\ 10^{-6}\ \pi\ w01\sim^2 \,/\, (\pi^2\ w01\sim^4 - 2.666666666\ \pi^2\ w01\sim^4\ z\sim$$
$$+ 1.777777777\ z\sim^2\ \pi^2\ w01\sim^4 + .1576089999\ 10^{-12}\ z\sim^2)$$

```
> Zr1:=evalf(Zr1);
```

$$Zr1 := .7913331623\ 10^7\ w01\sim^2$$

```
> z:=f/(1+(f/Zr1)^2);
```

$$z := \frac{.75}{1 + \frac{.8982635864\ 10^{-14}}{w01\sim^4}}$$

Again, we have to help Maple eliminate z in *Imag*.

```
> Imag:=subs(z=.75*1/(1+.8982635864e-14/w01^4),-
.3969999999e-6*Pi*w01^2/(Pi^2*w01^4-
2.666666666*Pi^2*w01^4*z+1.777777777*z^2*Pi^2*w01^4+.157608
9999e-12*z^2)):
```

The spot size at the beam waist in the cavity is given in Eq. 18 to be

```
> w02:=evalf((L*lambda/(2*Pi))^(1/2));
```

$$w02 := .0001805635854$$

Now we solve for the spot size at the lens:

```
> w01:=solve(Imag=-lambda/(Pi*w02^2),w01);
```

$$w01 := -.0004875742072, -.0002176887326 - .0002176887326\,I, -.0002176887326 + .0002176887326\,I, -.0001943842948, -9.028179285\,I, 9.028179285\,I, .0001943842948, .0002176887326 - .0002176887326\,I, .0002176887326 + .0002176887326\,I, .0004875742072$$

The real, positive answer should be correct.

```
>  w01:=.00048;
```

$$w01 := .00048$$

Now we compute z:

```
> z:=evalf(subs(w01=.00025,.5*1/(1+.3940224999e-
13/(Pi^2*w01^4))));
```

$$z := .4650268797$$

Finally, we find the Rayleigh range:

```
> Zr1:=subs(w01=.00025,7913331.623*w01^2);
```

$$Zr1 := 1.823231606$$

We conclude that the Gaussian mode is matched to the cavity by aperturing it to a spot size of 0.5mm and placing the f = 750mm lens a distance of 46.5cm from the confocal point.